PdAg Nanorings Supported on Graphene Nanosheets: Highly Methanol-Tolerant Cathode Electrocatalyst for Alkaline Fuel Cells

*Minmin Liu, Yizhong Lu, and Wei Chen**

Due to the high costs, slow reaction kinetics, and methanol poisoning of platinum-based cathode catalysts, designing and exploring non-Pt or low-Pt cathode electrocatalysts with a low cost, high catalytic performance, and high methanol-tolerance are crucial for the commercialization of fuel cells. Here, a facile method to fabricate a system of PdAg nanorings supported by graphene nanosheets is demonstrated; the fabrication is based on the galvanic displacement reaction between pre-synthesized Ag nanoparticles and palladium ions. X-ray diffraction and high-resolution transmission electron microscopy show that the synthesized PdAg nanocrystals exhibit a ring-shaped hollow structure with an average size of 27.49 nm and a wall thickness of 5.5 nm. Compared to the commercial Pd–C catalyst, the PdAg nanorings exhibit superior properties as a cathode electrocatalyst for oxygen reduction. Based on structural and electrochemical studies, these advantageous properties include efficient usage of noble metals and a high surface area because of the effective utilization of both the exterior and interior surfaces, high electrocatalytic performance for oxygen reduction from the synergistic effect of the alloyed PdAg crystalline phase, and most importantly, excellent tolerance of methanol crossover at high concentrations. It is anticipated that this synthesis of graphene-based PdAg nanorings will open up a new avenue for designing advanced electrocatalysts that are low in cost and that exhibit high catalytic performance for alkaline fuel cells.

1. Introduction

As one of the most promising clean energy sources for the future, direct methanol fuel cells (DMFCs) have received persistent attention in the past decades.[1] Compared to gas-powered fuel cells, DMFCs exhibit a number of advantages, such as high energy density, ease of storage and transport of liquid fuels, low operating temperature and pressure, lack of fuel reforming, and simple system design.[2] It is widely accepted that the overall performance and the cost of fuel cells are mainly dependent on the anode catalysts for fuel oxidation and the cathode catalysts for the oxygen reduction reaction (ORR). To realize the commercialization of fuel cells, much effort has been devoted to the design of novel nanostructured electrocatalysts.[3] To improve the catalytic activity and reduce the costs of electrocatalysts, various Pt-based alloyed nanomaterials, such as PtPd, PtRu, PtFe, PtCo, and PtNi,[4] have been fabricated and extensively investigated as anodic and cathodic electrocatalysts. Athough substantial progress has been achieved, some critical challenges remain to be overcome for platinum electrocatalysts on both the anode and cathode. First, with Pt-based materials as anode catalysts, self-poisoning due to the strong adsorption of CO intermediates onto Pt surface significantly reduces the catalytic performance. Second, a high overpotential arising from the sluggish electron-transfer kinetics significantly degrades the efficiency of fuel cells. On the other hand, methanol fuel molecules in DMFCs may easily crossover from the anode to cathode through the polymer electrolyte membranes and then react directly with the cathode catalyst. Such a process can reduce the ORR performance and thus further lower fuel efficiency because of the possible poisoning of the cathode catalysts and the formation of mixed potentials at the cathode. To address these key points, non-Pt metal catalysts, such as Pd-based nanomaterials, transition metal alloys,[5] transition metal oxides,[6] transition metal sulfides[7] and macrocyclic complexes,[8] precious metal nanoclusters, etc.,[3c,9] have been proposed as potential alternatives to Pt-based catalysts for fuel cells.

Up to now, Pd-based materials have been considered the promising alternative catalysts for both the anode and cathode of DMFCs because of their comparable catalytic properties but much lower cost relative to Pt-based materials. Since catalysis occurs only on the surface of catalysts, the surface structure and composition play crucial roles in determining the catalytic activity of a catalyst. For nanostructured electrocatalysts in particular, it has been found that their catalytic properties are also strongly dependent on the shape, core size, and surface composition of the nanomaterials.[10] For instance, Sun and co-workers[11] reported that tetrahexahedral Pt nanocrystals enclosed by 24 high-index facets exhibit enhanced catalytic activity for electro-oxidation of small organic fuels. As

M. M. Liu, Y. Z. Lu, Prof. W. Chen
State Key Laboratory of Electroanalytical Chemistry
Changchun Institute of Applied Chemistry
Chinese Academy of Sciences
5625 Renmin Street, Changchun, 130022, China
E-mail: weichen@ciac.jl.cn
M. M. Liu, Y. Z. Lu
Graduate School of the Chinese Academy of Sciences
Beijing 100039, China

DOI: 10.1002/adfm.201202225

for Pd-based nanomaterials, nanoparticles, -wires, -and rods and nanomaterials of other shapes have been synthesized and investigated as potential electrocatalysts.[12] To reduce the metal catalyst loading, the main techniques include reducing the particle size, alloying them with transition metals, and fabricating surface-area-enhanced nanostructures. For example, Lim et al.[13] synthesized bimetallic Pd–Pt nanodendrites structured with a dense array of Pt branches on a Pd core. With such a surface structure, the surface area is largely increased, resulting in superior mass catalytic activity for the ORR. Because only the atoms on the surface or sub-surface can provide the reactive sites for catalysis, the large quantities of bulk atoms located within the interior of the material are actually not involved in the catalysis reactions. As a result, precious metal materials with a hollow structure are of great interest in the application of catalysts; much less metal is needed to bring about the same catalytic activity compared to solid catalysts.[14] The galvanic replacement reaction is an effective method to prepare hollow metal nanostructures. Taking advantage of the different standard reduction potentials of Ag^+/Ag (+0.7991 V vs. NHE (versus the normal hydrogen electrode)) and Pd^{2+}/Pd (+0.915 V vs. NHE), heterostructured PdAg nanomaterials in a variety of shapes and sizes have been successfully fabricated.[15]

It should be noted that in practical fuel cell applications, electrocatalysts are dispersed on carbon materials that should have high electrical conductivity, high stability, and a large surface area for high dispersion of the catalysts. Commonly used carbon supports include the traditional carbon black, carbon nanotubes, and carbon nanofibers.[16] As a new carbon nanomaterial class consisting of only a single layer of carbon atoms, graphene has received widespread attention since its discovery in 2004.[17] Due to the large surface area, excellent thermal/chemical stability and high electrical conductivity, graphene has been proposed as a catalyst support for fuel cells and catalysis.[18] Previous reports on graphene-supported metal nanoparticles, however, mainly focused on solid mono- or bi-metallic nanocrystals.

In this study, we present a facile two-step approach to fabricate graphene nanosheets (GNs) that support PdAg alloy nanorings (denoted as PdAg–GNs). Although much work has been done on the preparation of PdAg electrocatalysts, previous studies mainly focused on solid, porous, or hollow PdAg and PtAg nanomaterials, including nanoparticles, nanoplates, nanowires, and nanoboxes.[12a,15a–c,19] There have been no previous reports on the synthesis of ring-shaped PdAg nanomaterials supported by graphene nanosheets. Moreover, in previous galvanic exchange reactions based on silver nanoparticles, only porous or hollow nanoparticles were formed. In the present study however, PdAg nanorings can be formed with the GNs acting as templates. With the synthesized ring-shaped hollow nanomaterials as the cathode catalyst for oxygen reduction, obvious advantages exist relative to traditional catalysts. The uniform dispersion on the GN support, the large surface area due to the availability of both the exterior and interior surfaces of a thin wall (~5.5 nm), and the PdAg alloy crystal structure not only promote the catalytic activity for the ORR, but they also significantly reduce the Pd loading in comparison with solid Pd catalysts. Moreover, the synthesized hybrid materials exhibit high methanol-tolerance during the ORR. Such a nanostructured material with high catalytic activity, low cost, and excellent methanol-tolerance is a promising non-Pt cathode electrocatalyst, and it exhibits a technologically significant application for direct methanol fuel cells.

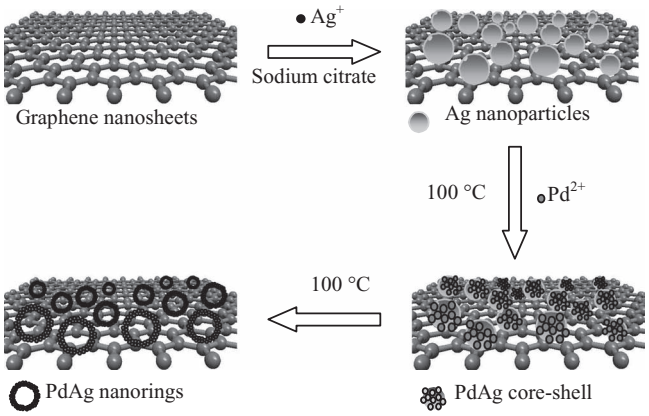

Scheme 1. Schematic illustrations of procedure for preparing graphene nanosheets supporting PdAg nanoring. The preparation involves a galvanic replacement reaction between the Ag nanoparticles and Pd^{2+} ions.

2. Results and Discussion

Graphene oxide nanosheets were prepared by a modified Hummers method.[20] Two steps were adopted to synthesize PdAg–GNs (**Scheme 1**). Firstly, Ag nanoparticles supported on graphene nanosheets (Ag–GNs) were synthesized by refluxing an aqueous mixture of silver nitrate and graphene oxide (GO) with sodium citrate as the reducing agent. In this process, the oxy-functional groups can act as nucleation sites and facilitate seeding and growth of the silver nanoparticles.[21] In the second step, nanocrystals comprising a Ag core and Pd shell were obtained through a galvanic replacement reaction between the Ag nanoparticles and Pd^{2+}. Previous scanning transmission microscopy (STM) and Auger electron spectroscopy (AES) studies showed that Ag atoms exhibit a strong tendency to diffuse from the bulk to the surface when they were alloyed with Pd.[22] In the present system, with the reaction proceeding, silver atoms in the core diffuse to the shell to form ring-shaped PdAg alloy nanostructures. **Figure 1**a shows the transmission electron microscopy (TEM) image of the synthesized GO. It can be seen that there is a uniform layer of GO with a wrinkled and folded morphology. Previous atomic force microscopy (AFM) studies have shown that only a single layer of a graphene nanosheet is formed.[23] Figure 1b and c show typical TEM images of the Ag–GNs and PdAg–GNs, respectively. In Figure 1b, the silver nanoparticles are seen to be uniformly dispersed on the GNs. After the galvanic reaction between the Ag–GNs and Pd^{2+}, the formed nanorings are evidently observed. From the particle size histograms shown in the insets of Figure 1b,c, the average diameters of the Ag nanoparticles and PdAg nanorings are determined to be 27.3 ± 6.3 and 27.5 ± 6.2 nm, respectively. The results indicated that although a hollow structure was formed during the galvanic replacement reaction, the particle size remains nearly unchanged. The formation of Ag–GNs and

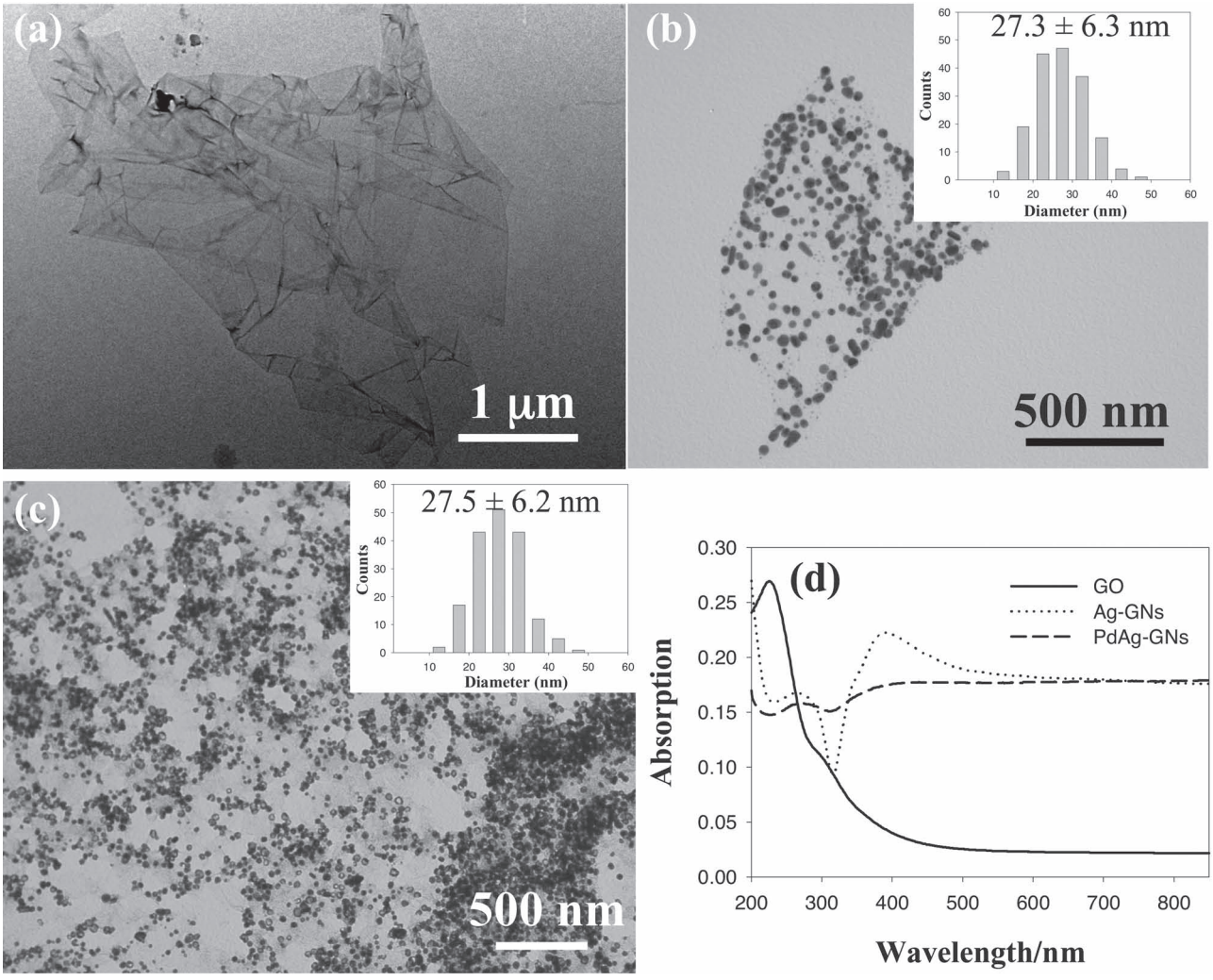

Figure 1. TEM images of the as-synthesized nanomaterials. a) Graphene oxide (GO); b) graphene-nanosheet-supported silver nanoparticles (Ag–GNs) and c) graphene-nanosheet-supported PdAg nanorings (PdAg–GNs). Insets in b and c show the corresponding diameter histograms of the Ag nanoparticles and PdAg nanorings. d) UV–vis absorption spectra of the synthesized GO, Ag-GNs, and PdAg–GNs.

PdAg–GNs was also characterized by UV–vis measurements. Figure 1d depicts the UV–vis absorption spectra of the Ag-GNs and PdAg–GNs as well as the as-prepared GO. In the UV–vis spectrum of GO, the absorption at 230 nm and the shoulder around 300 nm can be ascribed to the π–π^* transitions of the aromatic C=C bonds and the n–π^* transitions of the C=O bonds. With Ag nanoparticles formed on graphene nanosheets, there is obviously a new absorption peak at about 391 nm, corresponding to the typical surface plasmon absorption of Ag nanoparticles. As for the PdAg–GNs, the surface plasmon absorption decreases markedly and red-shifts to 437 nm due to the partial substitution of the Ag atoms by Pd atoms during the galvanic replacement reaction, also suggesting the formation of PdAg bimetallic nanocrystals.

To investigate the crystal structure and elemental distribution of the PdAg nanorings, high-resolution TEM (HRTEM) was also performed. **Figure 2**a and b show the HRTEM images of the

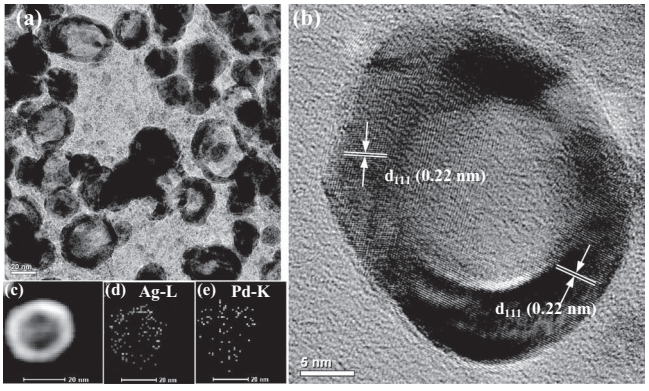

Figure 2. a,b) HRTEM images at different magnifications of the as-synthesized PdAg nanorings supported on a graphene nanosheet. c) HAADF microscopy image of a single PdAg nanoring and d,e) the corresponding elemental mapping for Ag (d) and Pd (e).

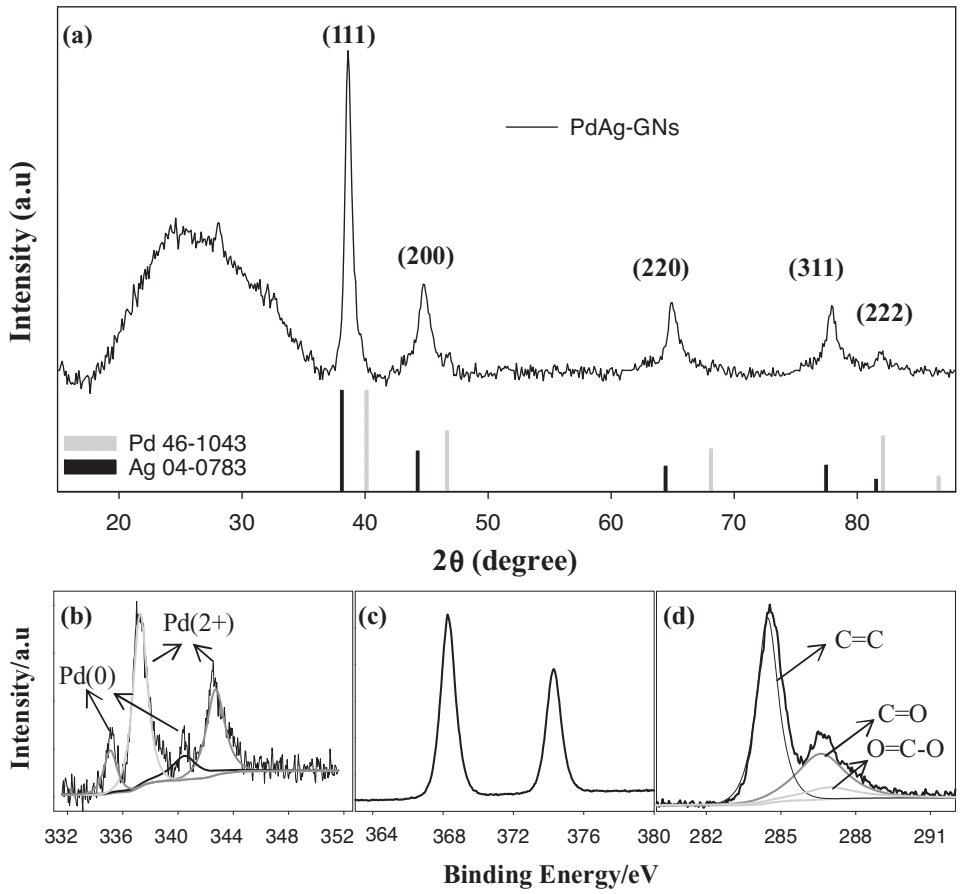

Figure 3. Structural characterization of the PdAg–GNs using X-ray techniques. a) XRD pattern of the as-synthesized PdAg–graphene. For comparison, the JCPDS patterns of bulk Pd and bulk Ag are also included. b–d) High-resolution X-ray photoelectron spectra of Pd 3d (b), Ag 3d (c), and C 1s (d).

prepared PdAg–GNs at different magnifications, from which the highly crystalline ring-shaped nanocrystals can be clearly observed. The average thickness of the ring wall is around 5.5 nm. From the HRTEM image of the single nanocrystal shown in Figure 2b and in Figure S1 of the Supporting Information (SI), well-resolved lattice fringes are present with an interplanar spacing of 0.22 nm, which can be indexed to the (111) plane of PdAg. For further insight into the distribution of the Pd and Ag in the PdAg nanorings, scanning transmission electron microscopy (STEM) was carried out for an elemental analysis. Figure 2c shows a high-angle annular dark-field (HAADF) microscopy image of a single nanoring. From the elemental maps of Ag and Pd shown in Figure 2d and e, respectively, a ring-shaped nanostructure with Ag and Pd evenly distributed throughout the shell was obviously produced. The energy dispersive X-ray (EDX) spectrum (Figure S2, SI) further indicates the presence of Ag and Pd in the PdAg–GNs product. Electron microscopy investigations suggest that the alloy structure was formed in the wall of the PdAg nanorings, which is further verified by X-ray characterization techniques. In the HRTEM images shown in Figure 2b and Figure S1 (SI), there are small clusters dispersed inside the nanorings. The EDX measurements (Figure S3, SI) that focused on this area showed that the clusters were silver nanoparticles.

Figure 3a shows the XRD pattern of the as-synthesized PdAg nanorings, from which five strong diffraction peaks could be indexed to the (111), (200), (220), (311), and (222) planes of the PdAg nanocrystals. It should be noted that compared to the patterns of bulk Pd (No. 46–1043, gray bars) and Ag (No. 04–0783, black bars) from the Joint Committee on Powder Diffraction Standards (JCPDS), the diffraction peaks from the synthesized PdAg nanocrystals are located between the diffraction peaks expected from pure Pd and Ag, strongly indicating the formation of an alloyed crystal structure. Both HRTEM and XRD results suggest that during the galvanic replacement reaction, silver atoms are likely to diffuse from the bulk to the ring wall to form alloyed hollow structures. In addition to the diffraction peaks from PdAg alloys, a broad peak around 25.5° corresponds to the characteristic diffraction peak (002) of the hexagonal structure of GNs. This indicates that graphene oxide has been reduced to graphene during the reduction process in which sodium citrate was reducing agent. The oxidation states of Pd, Ag, and the graphene support were investigated by X-ray photoelectron spectroscopy (XPS). Figure S4 in the SI shows the survey spectrum of the sample, which is dominated by the signals of Ag, Pd, C, and O. Figure 3b and c present the high-resolution XPS spectra of Pd and Ag. It can be seen that the XPS spectrum of Pd can be deconvoluted into four peaks at

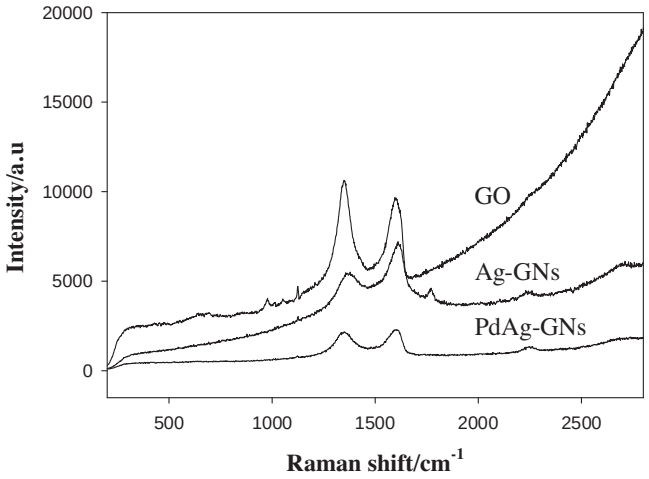

Figure 4. Raman spectra of GO and the Ag–GN and PdAg–GN composites.

around 335.13, 337.27, 340.47 and 342.69 eV, indicating that Pd is present in the ring-shaped nanocrystals as both metallic Pd and PdO. The XPS signals from the oxidation states of palladium may be from the partial adsorption of excessive Pd^{2+} precursor on the Ag–GNs. On the other hand, the observation of the Ag $3d_{5/2}$ and $3d_{3/2}$ peaks at 368.25 and 374.28 eV, respectively, indicates that Ag is mainly present in the metallic state. The deconvoluted C 1s spectrum is shown in Figure 3d. Based on previous studies, the three fitted peaks can be assigned to the binding energies of carbon in C=C/C–C, C–O(epoxy/hydroxyls), and C=O (carbonyl/ketone).[23] The predominant intensity of C=C/C–C also indicates that graphene oxide has been reduced to graphene by the sodium citrate treatment.

Raman spectroscopy is widely used to detect the ordered and disordered crystalline structure of graphene. **Figure 4** shows the Raman spectra of graphene oxide, Ag–GNs, and PdAg–GNs. For graphene oxide, the two peaks at 1369 and 1611 cm^{-1} can be assigned to the D- and G-band, respectively. For Ag–GNs and PdAg–GNs, these two bands red-shift to 1350 and 1597 cm^{-1}, respectively, suggesting an interaction between graphene and the metal particles or rings. The D-band is related to the vibrations of sp^3 carbon atoms of disordered graphene nanosheets, while the G-band arises from vibrations of sp^2 carbon atom domains of graphite. From Figure 4, the intensity ratios of D- and G-bands (I_D/I_G) from Ag–GNs and PdAg–GNs are obviously larger than that of graphene oxide (0.746 in GO to 1.099 in Ag–GNs), which confirming that most of the oxygenated groups have been removed during the reduction process, i.e., the reduction of GO, producing r-GO (reduced graphene oxide). On the other hand, the I_D/I_G ratio is inversely proportional to the reciprocal of the average crystallite size of graphite materials. The increase of the I_D/I_G ratio in Ag-GNs and PdAg–GNs compared to that of the original GO support also implies the decreased size of the in-plane sp^2 domains and the partially ordered crystal structure of resulting graphene nanosheet supports.

The electrocatalytic activity of the as-synthesized PdAg–GNs for the oxygen reduction reaction was evaluated with electrochemical measurements by depositing the PdAg–GNs on a glassy carbon electrode (referred to as PdAg–GNs/GC). The typical cyclic voltammogram (CV) of PdAg–GNs/GC measured in N_2-saturated 0.1 M $HClO_4$ is shown in **Figure 5**a. Similar to that of a commercial Pd–C catalyst (denoted as Pd–C/GC) shown in Figure 5b, the features of hydrogen adsorption and desorption can be observed in the low-potential region. In the negatively directed potential sweep, reduction current peaks of palladium oxide are present at 0.66 and 0.64 V (vs. reversible hydrogen electrode, RHE) on PdAg–GNs/GC and Pd–C/GC, respectively. The more positive reduction potential obtained from PdAg–GNs indicates that the as-synthesized hollow PdAg nanocrystals are more catalytically active than the commercial Pd–C catalyst for the ORR.

The electrocatalytic activity for the ORR and the methanol-tolerance of PdAg–GNs/GC are shown in Figure 5c. Compared to the CV recorded in N_2-saturated KOH solution (0.1 M), significantly enhanced reduction current can be observed in O_2-saturated electrolyte, indicating the high electrocatalytic activity of the PdAg–GNs towards the ORR. It should be noted that the voltammetric currents have been normalized to the real active surface area, i.e., electrochemically active surface area (EASA), calculated from the reduction charge of Pd oxide (424 μC cm^{-2}). As described in the Introduction, methanol poisoning of cathodic catalysts is one of the challenging problems in direct methanol fuel cells. Here, the methanol-tolerant property of the PdAg–GNs was studied by introducing different concentrations of methanol into O_2-saturated 0.1 M KOH. It can be seen from Figure 5c that, with methanol concentration increasing in the electrolyte, even to a very high concentration of 5.0 M, no obvious decrease of reduction current is observed for the ORR on PdAg–GNs. Such a high tolerance to methanol oxidation means that with PdAg–GNs as the cathode catalyst, high concentrations of methanol can be fed at the anode to improve the performance of fuel cells. Such a methanol-tolerance phenomena has been reported previously.[24] For instance, Wang et al.[24b] synthesized carbon-supported Pd-Pt alloy electrocatalysts and studied their catalytic activities for methanol-tolerant oxygen reduction. They found that for the Pt–C catalyst, there is an obvious methanol oxidation current in the presence of 0.5 M methanol in the electrolyte solution; however, no obvious methanol oxidation current was observed at the synthesized PdPt alloy catalysts. The high methanol-tolerance of the Pd-based bimetallic catalysts may be attributed to the weak competition reaction of methanol oxidation during the ORR, induced by the composition effect of alloys and the low catalytic activity of Pd components for methanol oxidation. Moreover, in our case, it is well known that the Ag component in the PdAg nanorings is poorly active for methanol oxidation. For comparison, Figure 5d shows the CVs of the ORR at Pd–C/GC with different concentrations of methanol. By comparing Figure 5c and d, there are at least two aspects that warrant attention. First, the reduction current density of the ORR obtained from PdAg–GNs is significantly larger than that from the commercial Pd–C catalyst. For example, the peak current density of ORR is 0.08 mA cm^{-2} at the Pd–C/GC electrode; however, the peak current density increases to 1.9 mA cm^{-2} at the PdAg–GNs/GC electrode, which is 24 times higher than that of the Pd–C catalyst. This result indicates that the prepared PdAg nanorings exhibit remarkably

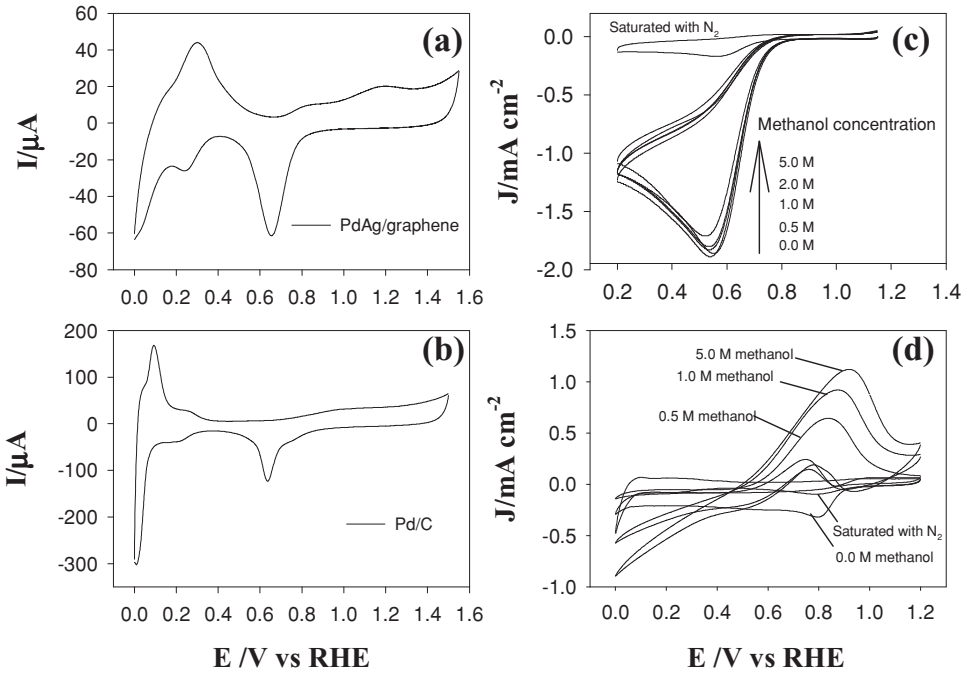

Figure 5. CVs of a) the synthesized PdAg–GNs/GC and b) commercial Pd–C/GC electrodes in 0.1 M $HClO_4$ solution; c) PdAg–GNs/GC in N_2- or O_2-saturated 0.1 M KOH solution containing 0.0, 0.5, 1.0, 2.0, and 5.0 M methanol; and d) Pd–C/GC in N_2- or O_2-saturated 0.1 M KOH solution containing 0.0, 0.5, 1.0, and 5.0 M methanol. A potential scan rate of 0.1 V s^{-1} was used for all CVs.

enhanced catalytic activity for the ORR in alkaline electrolyte. Such enhanced catalytic activity may be ascribed to the structurally synergistic effect between Pd and Ag as shown in the XRD pattern (Figure 3a). Second, contrary to the negligible ORR current change at PdAg–GNs/GC upon methanol addition in electrolyte, a very large oxidation current can be observed at the Pd–C catalyst with the addition of methanol. As shown in Figure 5d, the oxidation current densities increase with the methanol concentrations increasing, and almost no reduction current from ORR can be seen. The observed oxidation current was obviously attributed to the methanol oxidation catalyzed by Pd–C, suggesting that ORR on the commercial cathode Pd–C catalyst suffers heavily from methanol poisoning.

The catalytic performance of PdAg–GNs/GC was further compared with the commercial Pt–C catalyst (E-TEK, 20 wt% Pt on Vulcan XC-72 carbon). Figure S5a in the SI shows the CV of Pt–C/GC in 0.1 M $HClO_4$, in which the CV characteristics of Pt can be observed clearly. Comparing Figure S5b in the SI and Figure 5c reveals that although a larger ORR current density was obtained at Pt–C/GC, Pt–C/GC exhibited a much lower methanol-tolerance. It should be noted that the present study focuses on Pd-based materials; catalytic performance should be mainly compared to the commercial Pd–C catalyst. Moreover, previous studies showed that Pd-based catalysts possess similar catalytic activities for the ORR, but higher alcohol-tolerance than Pt-based catalyst.[25] The electrochemical results strongly suggest that the as-synthesized PdAg–GNs exhibit not only high catalytic activity for the ORR but also remarkably high tolerance towards methanol crossover. Moreover, from the XPS measurements, the average atom ratio of Pd to Ag is only 1:20, suggesting that only very low Pd loading is needed to gain the efficient ring-shaped PdAg–GNs electrocatalyst. High electrocatalytic performance with such low loading could be ascribed to the effective utilization of both the exterior and interior surfaces of the hollow structure with the thin ring wall; therefore, compared to commercial Pd–C catalyst, the present material appears to be a promising cathode catalyst for use in alkaline DMFCs. It should be pointed out that graphene plays two roles in the present study. First, graphene was used as a template to synthesize the PdAg nanorings. As described above, the oxyfunctional groups can act as nucleation sites for the formation of silver nanoparticles. Second, with the as-synthesized PdAg nanorings as electrocatalysts, graphene serves as catalyst support. Many reports in the literature have shown that graphene can be used as a support for electrocatalysts due to its large surface area, excellent stability, and highly electrical conductivity. In contrast, traditional carbon supports suffer from their electrochemical corrosion in fuel cells.

3. Conclusion

In summary, we have demonstrated a facile method to fabricate graphene-nanosheet-supported PdAg nanocrystals using the galvanic displacement reaction between pre-synthesized Ag nanoparticles and palladium ions. XRD and HRTEM show that the synthesized PdAg nanocrystals exhibit an interesting ring-shaped structure with an average size of 27.5 nm and a wall thickness of 5.5 nm. Compared to a commercial Pd–C catalyst, the graphene-supported hollow nanorings are superior as cathode electrocatalysts for oxygen reduction. Structural and electrochemical studies revealed that this system is

advantageous in several ways, including 1) efficient usage of noble metals and high surface areas, which arises because of the hollow nanostructure; 2) a high electrocatalytic performance for oxygen reduction due to the synergistic effect of the alloyed PdAg crystalline phase, and most importantly 3) an excellent tolerance to methanol crossover at high concentrations. It is anticipated that this synthesis of graphene-supported nanorings opens up a new avenue for designing advanced electrocatalysts with a low cost and a high catalytic performance for real alkaline fuel cell applications.

4. Experimental Section

Chemicals: Graphite powders (C, ≥98.0%, Tianjin Guangfu Delicacy Chemical Research Institute), sodium nitrate ($NaNO_3$, A.R. grade, ≥99.0%, Xilong Chemical Reagent), sulfuric acid (H_2SO_4, A.R. ~95–98%, Beijing Chemical Reagent), potassium permanganate ($KMnO_4$, A.R. grade, ≥99.8%, Beijing Chemical Reagent), hydrogen peroxide(H_2O_2, A.R. grade, ≥30%, Beijing Chemical Reagent), silver nitrate ($AgNO_3$, A.R. grade, ≥99.8%, Beijing Chemical Reagent), sodium citrate ($C_6H_5Na_3O_7 \cdot 2H_2O$, A.R. grade, ≥99.0%, Beijing Chemical Reagent), palladium nitrate ($Pd(NO_3)_2$, A.R. grade, Beijing Chemical Reagent), methanol (CH_3OH, A.R. grade, ≥99.5%, Beijing Chemical Reagent), and potassium hydroxide (KOH, A.R. grade, ≥85.0%, Beijing Chemical Reagent) were used as received without further purification. Ultrapure N_2 and O_2 were used for de-aeration and the oxygen reduction reaction, respectively. All aqueous solutions were prepared with ultrapure water supplied by a Water Purifier Nanopure water system (18.3 MΩ cm).

Synthesis of GO: GO was prepared using the modified Hummers and Offeman's method from graphite powders.[20] In brief, graphite powders (0.5 g) and $NaNO_3$ (0.5 g) were put into a clean flask, and concentrated H_2SO_4 (23 mL) was added with magnetic stirring for 10 min in an ice-water bath. $KMnO_4$ (3 g) was then slowly added into the solution. Once mixed, the solution was transferred to a 35 ± 5 °C oil bath and stirred for about 1 h. Next, water (40 mL) was added, and the resulting solution was stirred for another 30 min while the temperature was raised to 90 ± 5 °C. Then, more water (100 mL) was added, followed by a slow addition of H_2O_2 (3 mL, 30%). Finally, the warm solution was filtered and washed with water (100 mL) to remove the acid. The filter cake was then dispersed in water by mild sonication using a table-top ultrasonic cleaner. The products were then separated via centrifugation at a low-speed of 3000 rpm for 2 min. This process was repeated ~3–5 times to remove all visible particles. For the supernatant, two more high-speed centrifugation steps were carried out at 10 000 rpm for 10 min to remove all the byproduct soluble in water. The last sediment was re-dispersed in water with mild sonication, which resulted in homogeneous yellow solution of exfoliated GO.

Preparation of Ag–GNs and PdAg–GNs Composites: Ag nanoparticles supported on graphene nanosheets were prepared based on the procedure reported by Lee and Meisel.[26] The method was as follows: GO (2 mL, 2 mg mL^{-1}) was dispersed in pure water (23 mL) and then the solution was added into a clean 100 mL flask. The above solution was mixed by ultrasonic agitation in an oil bath for 10 min. After being added into sodium citrate (0.275 g), the solution was heated to boiling with magnetic stirring. After silver nitrate (0.0255 g) was added, the system was refluxed and stirred for 2.5 h, resulting in a solution color change from brown to dark brown. After cooling down to room temperature, the resulting dispersion was centrifuged at 10 000 rpm for 10 min and washed with pure water three times. The final precipitate obtained was re-dispersed in pure water and then heated to 100 °C with magnetic stirring in an oil bath; afterwards palladium nitrate (2 mg) was added to the flask. The solution was refluxed and stirred for another 30 min. The solution was then centrifuged at 10 000 rpm for 10 min and washed 3 times.

Material Characterization: UV–vis spectroscopy studies were performed with a Cary spectrometer using a 1-cm quartz cuvette with a resolution of 2 nm. The morphology and crystal structure of the PdAg alloy nanocrystals were characterized with a Hitachi H-600 transmission electron microscope operated at 100 kV. HRTEM and HAADF-STEM, elemental analysis mapping, and EDX were carried out on a JEM-2010(HR) microscope operated at 200 kV. XRD was performed on a PW 1700 Powder Diffractometer using Cu-Kα radiation with a Ni filter (λ = 0.154059 nm at 30 kV and 15 mA). XPS measurements were performed using a VG Thermo ESCALAB 250 spectrometer (VG Scientific) operated at 120 W. The binding energy was calibrated against the C 1s line.

Electrochemistry: Voltammetric measurements were carried out with a CHI 750D electrochemical workstation. A glassy carbon (GC) disk electrode (3.0 mm diameter) was first polished with alumina slurries (0.05 μm) and then cleaned by sonication in 0.1 M HNO_3, H_2SO_4, and Nanopure water for 10 min successively. A portion of the PdAg–GNs (0.7 mL) was mixed with 5 wt% Nafion solution (60 μL) by ultrasonication for a few seconds. After the ink formed homogeneously, the ink (10 μL) was dropped on the surface of the clean GC electrode with a micropipette and dried at room temperature. The ORR was examined by first bubbling the electrolyte solution with ultrahigh purity oxygen for at least 20 min and then blanketing the solution with an oxygen atmosphere during the entire experimental procedure. The rotating ring-disk voltammograms were collected on a Princeton Applied Research (PAR) Model 636 Ring-Disk electrode system. A conventional three-electrode system was used in all the electrochemical measurements. An Ag/AgCl (in 3 M aqueous NaCl) and a Pt coil were used as the reference and counter electrodes, respectively. All potentials were converted to be versus the reversible hydrogen electrode (vs. RHE). All electrochemical experiments were carried out at room temperature.

Supporting Information

Supporting Information is available from the Wiley Online Library or from the author.

Acknowledgements

This work was supported by the National Natural Science Foundation of China (Nos. 21043013, 21275136) and the Natural Science Foundation of Jilin province, China (No. 201215090).

Received: August 7, 2012
Published online: October 12, 2012

[1] a) M. S. Dresselhaus, I. L. Thomas, *Nature* **2001**, *414*, 332–337; b) S. Wasmus, A. Kuver, *J. Electroanal. Chem.* **1999**, *461*, 14–31; c) J. L. Zhang, Z. Xie, J. J. Zhang, Y. H. Tanga, C. J. Song, T. Navessin, Z. Q. Shi, D. T. Song, H. J. Wang, D. P. Wilkinson, Z. S. Liu, S. Holdcroft, *J. Power Sources* **2006**, *160*, 872–891.

[2] M. Winter, R. J. Brodd, *Chem. Rev.* **2004**, *104*, 4245–4269.

[3] a) C. Bianchini, P. K. Shen, *Chem. Rev.* **2009**, *109*, 4183–4206; b) A. C. Chen, P. Holt-Hindle, *Chem. Rev.* **2010**, *110*, 3767–3804; c) W. Chen, S. W. Chen, *Angew. Chem. Int. Ed.* **2009**, *48*, 4386–4389.

[4] a) W. Chen, J. Kim, S. H. Sun, S. W. Chen, *Phys. Chem. Chem. Phys.* **2006**, *8*, 2779–2786; b) V. R. Stamenkovic, B. Fowler, B. S. Mun, G. F. Wang, P. N. Ross, C. A. Lucas, N. M. Markovic, *Science* **2007**, *315*, 493–497; c) E. Antolini, J. R. C. Salgado, E. R. Gonzalez, *J. Power Sources* **2005**, *141*, 13–18; d) W. Chen, L. P. Xu, S. W. Chen, *J. Electroanal. Chem.* **2009**, *631*, 36–42; e) W. Chen, S. W. Chen, *J. Mater. Chem.* **2011**, *21*, 9169–9178.

[5] J. Sanabria-Chinchilla, K. Asazawa, T. Sakamoto, K. Yamada, H. Tanaka, P. Strasser, *J. Am. Chem. Soc.* **2011**, *133*, 5425–5431.

[6] Y. Liu, A. Ishihara, S. Mitsushima, N. Kamiya, K. Ota, *J. Electrochem. Soc.* **2007**, *154*, B664–B669.

[7] J. J. Diao, F. S. Qiu, G. D. Chen, M. E. Reeves, *J. Phys. D Appl. Phys.* **2003**, *36*, L25–L27.
[8] L. Zhang, J. J. Zhang, D. P. Wilkinson, H. J. Wang, *J. Power Sources* **2006**, *156*, 171–182.
[9] a) Y. Z. Lu, W. Chen, *J. Power Sources* **2012**, *197*, 107–110; b) W. Tang, H. F. Lin, A. Kleiman-Shwarsctein, G. D. Stucky, E. W. McFarland, *J. Phys. Chem. C* **2008**, *112*, 10515–10519; c) H. B. Wu, W. Chen, *J. Am. Chem. Soc.* **2011**, *133*, 15236–15239; d) W. T. Wei, Y. Z. Lu, W. Chen, S. W. Chen, *J. Am. Chem. Soc.* **2011**, *133*, 2060–2063.
[10] a) S. E. Habas, H. Lee, V. Radmilovic, G. A. Somorjai, P. Yang, *Nat. Mater.* **2007**, *6*, 692–697; b) W. Chen, J. M. Kim, S. H. Sun, S. W. Chen, *Langmuir* **2007**, *23*, 11303–11310.
[11] N. Tian, Z. Y. Zhou, S. G. Sun, Y. Ding, Z. L. Wang, *Science* **2007**, *316*, 732–735.
[12] a) Y. Z. Lu, W. Chen, *ACS Catal.* **2012**, *2*, 84–90; b) F. L. Jia, K. W. Wong, L. Z. Zhang, *J. Phys. Chem. C* **2009**, *113*, 7200–7206; c) X. G. Wang, W. M. Wang, Z. Qi, C. C. Zhao, H. Ji, Z. H. Zhang, *J. Power Sources* **2010**, *195*, 6740–6747; d) Z. Yin, H. J. Zheng, D. Ma, X. H. Bao, *J. Phys. Chem. C* **2009**, *113*, 1001–1005.
[13] B. Lim, M. J. Jiang, P. H. C. Camargo, E. C. Cho, J. Tao, X. M. Lu, Y. M. Zhu, Y. N. Xia, *Science* **2009**, *324*, 1302–1305.
[14] a) H. P. Liang, H. M. Zhang, J. S. Hu, Y. G. Guo, L. J. Wan, C. L. Bai, *Angew. Chem. Int. Ed.* **2004**, *43*, 1540–1543; b) X. W. Lou, L. A. Archer, Z. C. Yang, *Adv. Mater.* **2008**, *20*, 3987–4019.
[15] a) Y. G. Sun, B. T. Mayers, Y. N. Xia, *Nano Lett.* **2002**, *2*, 481–485; b) Y. Z. Lu, W. Chen, *J. Phys. Chem. C* **2010**, *114*, 21190–21200; c) Y. G. Sun, Z. L. Tao, J. Chen, T. Herricks, Y. N. Xia, *J. Am. Chem. Soc.* **2004**, *126*, 5940–5941; d) Y. Z. Lu, R. T. Jin, W. Chen, *Nanoscale* **2011**, *3*, 2476–2480.
[16] Y. J. Wang, D. P. Wilkinson, J. J. Zhang, *Chem. Rev.* **2011**, *111*, 7625–7651.
[17] K. S. Novoselov, A. K. Geim, S. V. Morozov, D. Jiang, Y. Zhang, S. V. Dubonos, I. V. Grigorieva, A. A. Firsov, *Science* **2004**, *306*, 666–669.
[18] S. J. Guo, S. J. Dong, *Chem. Soc. Rev.* **2011**, *40*, 2644–2672.
[19] a) J. Y. Chen, B. Wiley, J. McLellan, Y. J. Xiong, Z. Y. Li, Y. N. Xia, *Nano Lett.* **2005**, *5*, 2058–2062; b) C. L. Lee, C. M. Tseng, *J. Phys. Chem. C* **2008**, *112*, 13342–13345.
[20] W. S. Hummers, R. E. Offeman, *J. Am. Chem. Soc.* **1958**, *80*, 1339–1339.
[21] R. Zan, U. Bangert, Q. Ramasse, K. S. Novoselov, *J. Phys. Chem. Lett.* **2012**, *3*, 953–958.
[22] a) P. T. Wouda, M. Schmid, B. E. Nieuwenhuys, P. Varga, *Surf. Sci.* **1998**, *417*, 292–300; b) H. Amandusson, L. G. Ekedahl, H. Dannetun, *J. Membrane Sci.* **2001**, *193*, 35–47.
[23] Y. Z. Lu, Y. Y. Jiang, W. T. Wei, H. B. Wu, M. M. Liu, L. Niu, W. Chen, *J. Mater. Chem.* **2012**, *22*, 2929–2934.
[24] a) D. L. Wang, H. L. L. Xin, H. S. Wang, Y. C. Yu, E. Rus, D. A. Muller, F. J. DiSalvo, H. D. Abruna, *Chem. Mater.* **2012**, *24*, 2274–2281; b) W. M. Wang, Q. H. Huang, J. Y. Liu, Z. Q. Zou, Z. L. Li, H. Yang, *Electrochem. Commun.* **2008**, *10*, 1396–1399.
[25] E. Antolini, *Energy Environ. Sci.* **2009**, *2*, 915–931.
[26] P. C. Lee, D. Meisel, *J. Phys. Chem.* **1982**, *86*, 3391–3395.